Data-driven discovery and synthesis of high entropy alloy hydrides with targeted thermodynamic stability

Matthew Witman,[*,†,§] Gustav Ek,[‡,§] Sanliang Ling,[¶,§] Jeffery Chames,[†] Sapan Agarwal,[†] Justin Wong,[†] Mark D. Allendorf,[†] Martin Sahlberg,[*,‡] and Vitalie Stavila[*,†]

[†]Sandia National Laboratories, Livermore, California 94551, United States
[‡]Department of Chemistry - Ångström Laboratory, Uppsala University, Box 523, SE-75120, Uppsala, Sweden
[¶]Advanced Materials Research Group, Faculty of Engineering, University of Nottingham, University Park, Nottingham, NG7 2RD, UK
[§]Contributed equally to this work

E-mail: mwitman@sandia.gov; martin.sahlberg@kemi.uu.se; vnstavi@sandia.gov

Abstract

Solid-state hydrogen storage materials that are optimized for specific use cases could be a crucial facilitator of the hydrogen economy transition. Yet the discovery of novel hydriding materials has historically been a manual process driven by chemical intuition or experimental trial-and-error. Data-driven materials' discovery paradigms provide an alternative to traditional approaches, whereby machine/statistical learning (ML) models are used to efficiently screen materials for desired properties and significantly narrow the scope of expensive/time-consuming first-principles modeling and experimental validation. Here we specifically focus on a relatively new class of hydrogen storage materials, high entropy alloy (HEA) hydrides, whose vast combinatorial composition space and local structural disorder necessitates a data-driven approach that does not rely on exact crystal structures in order to make property predictions. Our ML model quickly screens hydride stability within a large HEA space and permits down selection for laboratory validation based not only on targeted thermodynamic properties, but also secondary criteria such as alloy phase stability and density. To experimentally verify our predictions, we performed targeted synthesis and characterization of several novel hydrides that demonstrate significant destabilization (70x increase in equilibrium pressure, 20 kJ/molH$_2$ decrease in desorption enthalpy) relative to the benchmark HEA hydride, TiVZrNbHfH$_x$. Ultimately, by providing a large composition space in which hydride thermodynamics can be continuously tuned over a wide range, this work will enable efficient materials selection for various applications, especially in areas such as metal hydride based hydrogen compressors, actuators, and heat pumps.

Introduction

A transition to cleaner fuel sources that drastically reduce or altogether eliminate the release of harmful emissions is urgent.[1] With an energy density of 120 MJ/kg that is three times that of gasoline, hydrogen is perhaps the ultimate clean fuel. When used in a fuel cell, the only

point-of-use emission product is water, thereby avoiding emissions associated with fossil fuel combustion (CO_2, NO_x, SO_x, particulate matter, etc.).[2] However, several technical barriers have limited the roll-out of a hydrogen-powered economy, several of the most prominent being the difficulty of economically and safely storing, pressurizing, and/or transporting H_2.[3]

Metal hydrides have long been investigated as promising candidates for hydrogen storage, and their hydriding thermodynamics vary widely.[4–6] For example, TiFe hydrogenates reversibly near ambient conditions but, typical of intermetallic compounds composed of heavy 3d transition metals, has a relatively low hydrogen weight capacity and is therefore better suited for stationary (rather than vehicular) storage applications.[7] Complex hydrides[8;9] on the other hand are much lighter with much larger enthalpies of desorption, typically requiring extremely high temperatures (hundreds of °C) for hydrogen release. While alloying/doping[10–14] and nanoscaling[15–18] can destabilize these complex hydrides, it has generally been difficult to design a metal hydride that satisfies the delicate trade-off between appropriate thermodynamic stability and sufficiently high capacity (in addition to other desirable features like fast kinetics of dehydrogenation, reversibility, etc.). A relatively new class of materials known as high entropy alloys (HEAs), which have demonstrated usefulness in many applications,[19–25] have recently been investigated as hydrogen storage materials, demonstrating outstanding hydrogen-to-metal ratios (H/M > 2) and reversible weight capacities comparable to TiFe.[26] Combined, these properties portend their usefulness in a variety of hydrogen storage applications. Addressing their vast possible compositional space in the search of novel, high-performing hydrides is therefore the focus of this work.

Typically the search for new hydriding materials has been a manual one driven by the chemical intuition, expert knowledge, and design rules acquired over decades of data collection.[27–29] An emerging alternative utilizes a data-driven materials discovery approach facilitated by machine/statistical learning (ML) models, provided an adequate quantity of training data has been generated or extracted from the literature.[30,31] Once sufficiently trained, these models are many orders of magnitude faster to execute than experiments and can be used to quickly screen materials' space and discover novel high-performing candidates. This paradigm could greatly aid in the discovery of novel HEAs for hydrogen storage for several reasons. First, the HEA composition space grows combinatorially with the number of possible principal elements in the alloy, and therefore presents an intractable number of materials for brute-force synthesis or even density functional theory (DFT)-based screening. The solid solution (SS) disorder in HEAs must be sampled or accounted for, so DFT calculated properties based on a single random distribution of elements on the lattice may not be sufficiently accurate. Furthermore, prediction of the equilibrium hydriding pressure requires simulating the system in an open ensemble, which is rarely done at the DFT level of theory,[32] let alone for hundreds or thousands of materials. Therefore, a model that does not explicitly depend on crystal structure (so-called compositional ML models[33–35]) that can rapidly predict hydriding thermodynamics would greatly facilitate the rapid discovery of new HEA hydride candidates.

Specifically, we focus on a synergistic approach to materials discovery, whereby we first utilize ML-enabled high-throughput screening to quickly predict hydride stability for a novel dataset of HEA candidates. Since the interpretability of our compositional-ML model has recently elucidated a simple design rule,[31] we can even perform *a priori* selection of candidates with a desired thermodynamic stability simply based on features derived solely from their proposed composition. This exercise reveals that the equilibrium pressure of the HEA hydrides in the dataset spans many orders of magnitude and signifies usefulness in a variety of applications, from H_2-getters[36] to storage materials. Several of these novel HEA compositions were rationally selected (based on the ML model-based design rule), synthesized, and hydrogenated to demonstrate the large destabi-

lization that can be induced through compositional modifications within the dataset. Extensive DFT calculations validate the same design rule while adding additional physical insight, albeit at greater computational cost (i.e. requiring significant time on high performance computing resources, whereas the machine learning models applied herein can be trained and executed with just a desktop machine). Ultimately, this demonstrates that the thermodynamic stability can be *a priori* predicted and continuously tuned over a large window within this HEA material set. Both are necessities, for example, to enable technologies like metal hydride hydrogen compressors.[37,38]

Methods

HEA synthesis. The alloys were synthesized by melting lumps of Ti (Goodfellow, 99.99% metals basis), V (ChemPur, 99.9% metals basis), Nb (Alfa Aesar, 99.95% metals basis), Zr (Chempur, 99.8% metals basis, excluding Hf), Hf (Chempur, 99.8% metals basis, maximum 4% Zr), Ta (Goodfellow, 99.9% metals basis), Cr (Alfa Aesar, 99.995% metals basis), Mo (Goodfellow, 99.9% metals basis), Al (Gränges, 99.999% metals basis), Pd (Hereaus, 99.9% metals basis) in an electric arc furnace in Ar atmosphere. Elements with low vapor pressure (Al, Cr) were pre-alloyed before final synthesis to avoid evaporation. To ensure chemical homogeneity, the samples were remelted five times and flipped between each melting. The mass losses were in all cases less than 0.1 wt% and thus the resultant composition can be considered very close to the nominal. Some of the ingots were then filed to powder with a metal file for X-ray diffraction analysis and the rest cut into smaller pieces for hydrogenation.

X-ray diffraction. Laboratory X-ray diffraction (XRD) was carried out on a Bruker D8 advance with Cu Kα radiation equipped with a LynxEye XE-T detector operating in Bragg-Brentano geometry, with the powders placed on zero-background Si-wafer sample holders. The data was analyzed by the Ri-

etveld method implemented in the software Topas v6 Academic.[39] Peak shapes were modelled by Thompson-Cox-Hastings pseudo Voigt function[40] and the background by a six-order Chebyshev polynomial. Site occupancies were fixed to the nominal composition in all cases.

Energy Dispersive X-Ray Spectroscopy. A JEOL JSM-7600F Thermal Field Emission Electron Microscope was used to obtain SEM images, and an Oxford X-Max 80 detector with Aztec Software was used to obtain Energy Dispersive X-Ray Spectroscopy (EDS) maps. The conditions for both the SEM images and the EDS maps were: HT = 15kV, WD(nominal) = 8mm, Probe setting = 6. The sample was deposited onto carbon tape on an Aluminum stub, and no coating was applied. Areas chosen for analysis were fairly level and flat for best imaging results. This also pertains to obtaining the best EDS detection (count rate), as dramatic topography often results in shadowing that may be interpreted as an area depleted in an element.

PCT data collection. Pressure composition-temperature (PCT) isotherms were collected using a Setaram PCTPro instrument. Samples were loaded into high-pressure vessels, sealed with stainless-steel gaskets, and put under vacuum before thermal activation at 753 K. The thermocouple measuring the temperature is located outside of the stainless-steel pressure vessel in a thermocouple well to minimize the thermal gradients between the samples and the vessel exterior. The pressure transducers had an accuracy of $\pm 1\%$. The PCT experiments were conducted isothermally between 562 to 609 K to ensure that the kinetics of hydrogen uptake are fast enough to reach chemical equilibrium.

Computational methods. The machine learning models, specifically gradient boosting tree regressors and classifiers, presented herein were implemented using the scikit-learn library.[41] The Jupyter notebooks to reproduce all models and results exactly (using the same

hyperparamters and random seeds) are provided in Section S4, and additional details on the models are provided in Section S1 and Section S2. All DFT calculations were performed using the Vienna Ab initio Simulation Package,[42] with additional details on DFT settings summarized in Section S3.

Results and discussion

Enumerating the HEA design space. HEAs based on refractory metals have shown significant promise for hydrogen storage due to their propensity for high H/M ratios, high volumetric capacities, and reversibility,[43,44] although these properties depend significantly on alloy synthesis techniques and activation procedures.[45] While lower in gravimetric capacity than typical complex hydrides, they may prove practical for various applications due to these aforementioned advantages. Furthermore, the vast compositional tunability of HEAs provides a wide space for chemical exploration to further optimize their properties. We enumerate all equimolar 4-, 5-, and 6-element high entropy alloys from the set $E = \{$Al, Ti, V, Cr, Zr, Nb, Mo, Pd, Hf, Ta$\}$. These are mainly refractory metals (which tend to be widely studied for use in hydrogen absorbing HEAs[46]) with several other elements included that have demonstrated solid solution HEA formation with refractory metals.[47] Off-equimolar compositions could be identically incorporated into this screening workflow, we simply omit them for now since it would lead to an even greater explosion of possible chemical space. For convenience we will call this space of 672 compositions the refractory (rHEA) data set.

$$\text{rHEA} = \binom{E}{4} + \binom{E}{5} + \binom{E}{6} \qquad (1)$$

An improved ML model for hydride thermodynamics. In previous work[31] we trained gradient boosting tree (GBT)[41,48] regressor models to predict the thermodynamic properties of metal hydrides. The training data was derived by thoroughly cleaning and curating the HydPARK database, a historical repository of ∼2700 entries for alloy and intermetallic compositions and their experimental hydriding properties. Duplicate or incomplete entries whose hydride dissociation enthalpy (ΔH) and entropy (ΔS) could not be ascertained were discarded, leaving only ∼400 materials for the "ML-ready" HydPARK database.[31] We then computed the equilibrium pressure, $\ln(P_{eq}/P_o)$, as our ML target property via

$$\ln\left(P_{eq}/P_o\right) = -\frac{\Delta H}{RT} + \frac{\Delta S}{R}. \qquad (2)$$

P_o is the reference pressure of 1 bar, and, assuming temperature independence of ΔH and ΔS, we standardize our target property at 25 °C across all materials, denoted by $\ln(P_{eq}^o/P_o)$. Note that the GBT model cannot predict values outside the range of the target property observed in the training set. The fixed-length feature vector, $\mathbf{x} \in \mathbb{R}^{145}$, used to describe each material was computed using Magpie[33] and derives solely from the alloy composition. The ability to make these thermodynamic predictions without knowing the exact crystal structure is paramount given the solid solution character of HEAs and since rigorous computational prediction of an open ensemble observable like $\ln(P_{eq}^o/P_o)$ using an *ab initio* potential energy surface for hundreds of materials is infeasible.

Before proceeding with the rHEA screening, we improve upon the aforementioned model. First, we add two new training examples to the HydPARK database, corresponding to two rHEA alloys (TiVZrNbHf and TiVZrNb) whose hydriding thermodynamics were previously reported in the literature.[46] We refer to this slightly expanded training set as the HydPARK+ database. As discussed in Section S1.3, these materials introduce additional examples to the training data in a low frequency regime of the feature that is most important to the model, which heuristically explains why a model trained on HydPARK+ produces systematically shifted predictions (see Figure 1). The only way to validate the model's accuracy for this unlabeled dataset is to experimentally synthesize and obtain novel rHEA ther-

modynamic data, the ultimate objective of this work. The second model improvement comes from the addition of new composition-derived features. For all X elements contained across all HydPARK+ compositions, we extract the Materials Project computed[49,50] formation enthalpy per atom of the most stable binary hydride structure, $\Delta H_{bh,X}$. For each HydPARK+ composition, we then compute the composition-weighted average binary hydride formation enthalpy per atom,

$$\Delta \bar{H}_{bh} = \sum_i f_i \Delta H_{bh,i}, \qquad (3)$$

where f_i is the composition fraction of element i. This is combined with the Magpie features and helps improve the model's ability to predict ΔS, for example (see Section S1). The mean absolute error (MAE) of the $\ln(P_{eq}^o/P_o)$ and ΔH predictions of the original model are 1.5 and 6.1 kJ/molH$_2$, respectively. Our new model trained on HydPARK+ with this feature addition modestly decreases the error to 1.4 and 5.5 kJ/molH$_2$, respectively. More model training details and comparisons to the accuracy of previous models are provided in Section S1.

Wide ranging stability of rHEA hydrides. Using the new HydPARK+ ML model, Figure 1a plots the predictions of $\ln(P_{eq}^o/P_o)$ and ΔH for all rHEA hydrides versus the feature identified as most important by the GBT model,

$$\bar{\nu}_{pa} = \sum_i f_i \nu_{pa,i}. \qquad (4)$$

Here $\nu_{pa,i}$ is the ground state volume per atom of the elemental solid (see Ref. 31 for more discussion on physical interpretation of feature importance). Each material is color coded by its molecular weight. Star markers indicate previously reported HEA hydrides,[43] although measurement of ΔH and ΔS have only been reported for a few structures, which is why we plot their ML predicted values in Figure 1a. The original benchmark HEA hydride, TiVZrNbHfH$_x$, actually corresponds to one of the most stable hydrides in the rHEA dataset, and so we target novel, destabilized hydrides

with square markers in this work. While this GBT model is significantly more complex (and accurate, see Section S1) than a simple linear model with $\bar{\nu}_{pa}$ as the sole feature, we can generally target novel HEA hydrides with greater destabilization by considering compositions with smaller $\bar{\nu}_{pa}$. Such insights can only be derived when utilizing ML techniques that afford some degree of interpretability. The predictions of a ΔH model are also shown in Figure 1a vs. $\bar{\nu}_{pa}$, demonstrating the rHEA dataset spans a stability window of $\sim$35 kJ/molH$_2$.

Figure 1b shows that the rHEA predicted thermodynamics are systematically affected by the additional data in HydPARK+. Specifically, the original model under-predicts hydride stability (low $\ln(P_{eq}^o/P_o)$, high ΔH, low ΔS materials) relative to the HydPARK+ model. In Section S1.3 we rationalize this systematic shift as a consequence of these additional materials occupying a low-frequency region of $\bar{\nu}_{pa}$ space in the training data. After synthesizing and collecting the thermodynamic properties of the materials proposed in Figure 1a (the objective of this work), we can anticipate successively improved general accuracy of the ML thermodynamics model for future materials selection.

Figure 1c summarizes a global view of the SHapley Additive exPlanations (SHAP) values[51,52] for the $\ln(P_{eq}^o/P_o)$ model. Briefly, a SHAP value is computed for each feature of each material instance; this specifies how an instance's feature value "forces" the model's prediction to deviate from a baseline value. In this case, the baseline value is just the mean of the target value predictions across the entire dataset. The top and bottom plots show the SHAP values for the model trained on either the original HydPARK or HydPARK+ with additional features, respectively. Each marker represents a SHAP value (given by the x-coordinate) for a given feature (y-axis label) and rHEA instance. In other words, there are 672 SHAP values plotted per row, corresponding to the total number of rHEAs in the dataset. Each SHAP value is color-coded by its corresponding feature value. Note that only 9 out of the 145 most important features (as quantified by the sum of all SHAP values for each feature)
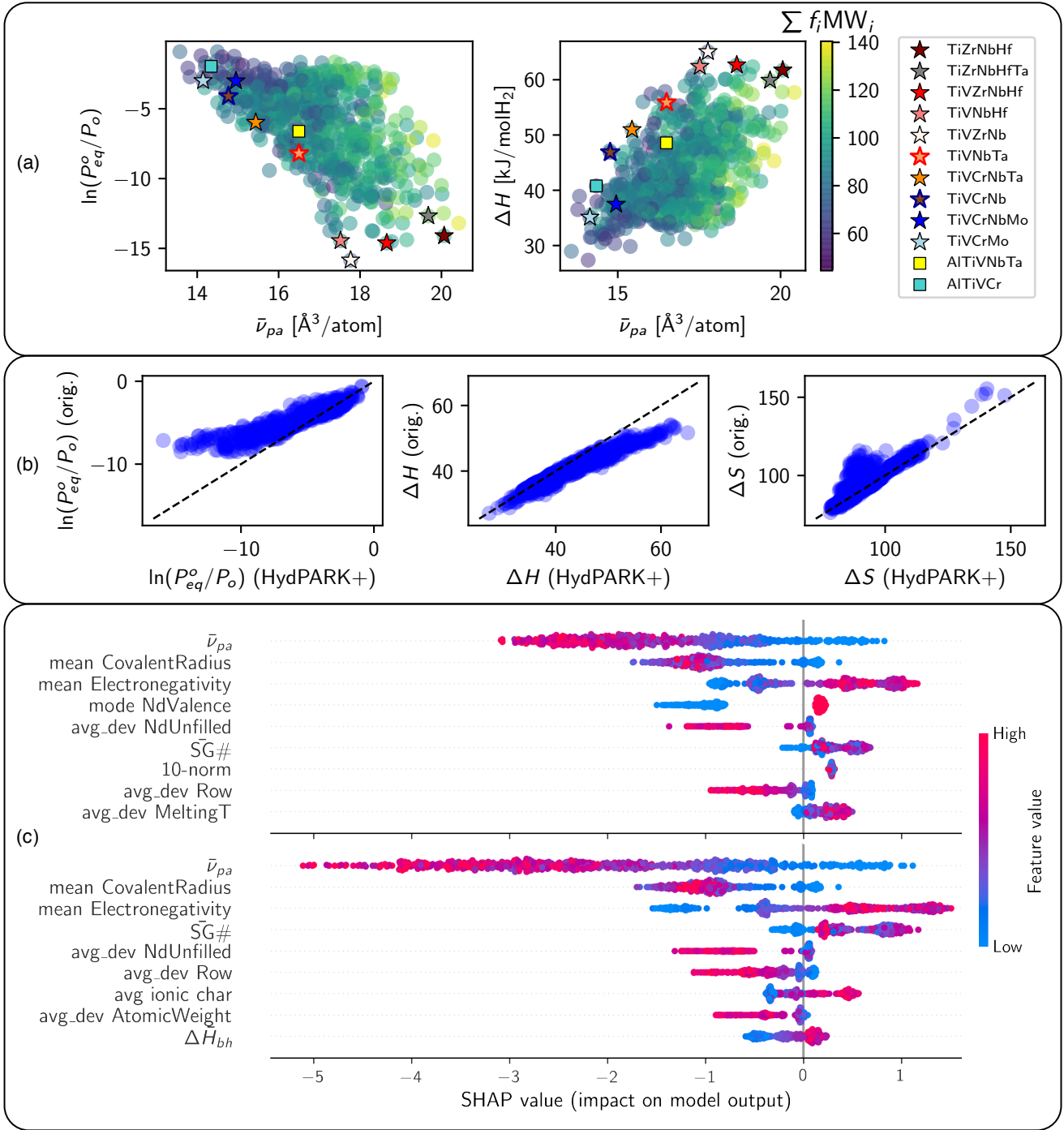
Figure 1: (a) ML-predicted $\ln(P_{eq}^o/P_o)$ and ΔH vs. $\bar{\nu}_{pa}$ for the rHEA dataset. Stars represent materials previously synthesized and tested for H_2 uptake while squares represent new candidates identified in this work. (b) Parity plots between rHEA thermodynamic predictions when using a model trained on the original HydPARK dataset vs. the HydPARK+ dataset (dashed black line corresponds to $y = x$). Enthalpy change, ΔH, is in units of $[kJ/molH_2]$ and entropy change, ΔS, is in units of $[J/(molH_2\ K)]$. (c) SHAP values for $\ln(P_{eq}^o/P_o)$ predictions on the rHEA dataset for models trained on the original HydPARK (top) and HydPARK+ (bottom) datasets. Note that for Magpie features not explicitly defined here, a detailed explanation can be found in Ref. 33.

are displayed here.

The new model's qualitative structure re-

mains relatively unchanged for the most important features; the change in equilibrium pres-

sure predictions observed in Figure 1b mainly arises from a re-scaling of the model's dependence on $\bar{\nu}_{pa}$. This arises since the equilibrium pressure is a function of ΔH and ΔS, and ΔH subsequently depends strongly on $\bar{\nu}_{pa}$ (Section S1). The model's predictions change more subtly with respect to some of the less important features. The additional feature's value becomes evident with the emergence of $\Delta \bar{H}_{bh}$, the second most important feature in the prediction of ΔS (Section S1). $\bar{SG\#} = \sum_i f_i SG\#_i$, where $SG\#_i$ is the space group number of ground state elemental solid i, is also highlighted in Figure 1c since it is the most important feature in the prediction of ΔS (Figure S1).

Phase selection from explainable classifiers. Synthesis of single-phase, body-centered cubic (BCC) SS alloys is an attractive starting point for designing high capacity hydrides.[53] Therefore, an additional model that predicts whether a given HEA composition forms a thermodynamically stable single-phase SS could be a useful filter before testing its hydriding properties. One approach involves high-throughput CALPHAD calculations based on experimental data, yet the expected accuracy decreases with increasing number of elements due to the expansive amount of experimental data required.[54,55] SS forming ability could be calculated from *ab initio* MD/MC,[56] but this again quickly becomes intractable (i.e. computing free energies of disordered, many-component solids) for more than just a handful of materials.

A simpler approach to deal with many component HEAs involves learning directly from experimental data such as the database compiled by Miracle et al.,[47] which includes all HEAs studied before 2015. The authors compiled ~ 400 literature reported compositions and whether the given compound forms an intermetallic (IM), an impure mixture of IM+SS, or a single-phase SS. Deriving empirical rules[56–58] or training statistical models[59] to predict the SS forming ability based on these literature reports presents a more computationally feasible approach.

We train a GBT classifier and an Aver-aged Weights for Explainable Machine Learning (AWE-ML) classifier[60] to predict whether a given composition is likely to exhibit a stable SS, SS+IM, or IM phase using the Miracle et al. database.[47] Details of the classifiers' training and performance are provided in Section S2. We then classify the rHEA dataset with both models, and Figure 2a shows the confusion matrix between the AWE-ML and GBT class predictions. Rows correspond to a GBT prediction, while columns correspond to AWE-ML predictions; therefore, 74% of rHEA materials are jointly predicted as having single-phase SS by the two models. This indicates both higher confidence in these predictions and that a significant portion of the rHEA dataset forms a stable SS phase, which has also been typical in experimental observations.[43,46] While the rHEA compounds represent a new, unlabeled dataset due to their lack of overlap with the Miracle et al. training data, a small scale validation can be performed using the more recently synthesized compounds (highlighted by stars in Figure 1a). All 10 of these alloys show an experimentally validated single-phase SS, and the GBT vs. AWE-ML confusion matrix is shown again in Figure 2b for these 10 compounds. Thus, the GBT and AWE-ML models have a classification accuracy of 80% and 70%, respectively, within this limited hold out set. We can therefore further down-select HEA candidates for hydrogenation experiments based on additional requirements, such as SS forming ability, with reasonable accuracy.

Synthesis of novel HEA hydrides. Novel rHEA compositions were selected for alloy synthesis and hydriding experiments based on ML predictions of the alloy's single-phase SS stability and the hydride's thermodynamic stability (using the HydPARK+ augmented model). Final candidates include AlTiVNbTa and AlTiVCr due to their predicted destabilization, i.e. higher $\ln(P_{eq}^o/P_o)$, relative to the benchmark TiVZrNbHf system and since they conveniently include lighter-weight, lower-cost aluminum. AlTiVNbTa was chosen for synthesis due to predicted modest destabilization ($\Delta H \sim$ 50 kJ/molH$_2$) and AlTiVCr due to significant
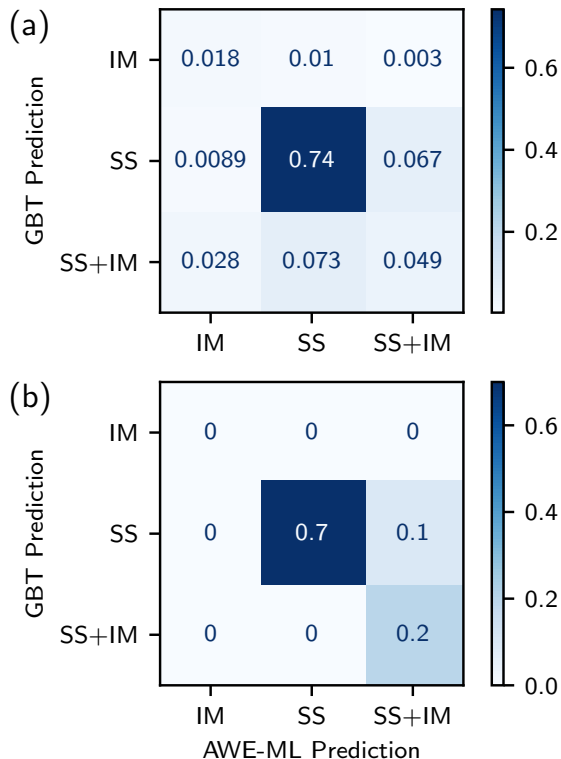
Figure 2: (a) Confusion matrix between AWE-ML and GBT predicted classes for the rHEA dataset, normalized over all 672 compositions. (b) Confusion matrix between AWE-ML and GBT predicted classes for the 10 previously synthesized compounds highlighted in Figure 1a, all of which have experimentally validated SS phases.

Table 1: Atomic percents of the as synthesized alloy and post-hydrided sample for AlTiVNbTa and AlTiVCr corresponding to the complete spectra in Section S5.2.2.

	AlTiVNbTa		AlTiVCr	
Element	Alloy	Post-H_2	Alloy	Post-H_2
Al	20.8	21.1	25.7	29.6
Ti	20.4	20.0	23.3	24.0
V	20.4	20.0	22.0	24.3
Cr	-	-	28.8	22.1
Nb	22.4	22.5	-	-
Ta	16.0	16.4	-	-

For each material, a van't Hoff analysis (Section S5.3.2) was used to obtain ΔH and ΔS, which can in turn be used to compute $\ln(P_{eq}^o/P_o)$. Experimental measurements vs. ML-predicted values are shown in the left column of Figure 3d (note that we also included recent thermodynamic measurements on TiVCrNb from Ref. 61 for comparison). Most importantly, the ML model correctly predicts the experimentally observed destabilization trend in $\ln(P_{eq}^o/P_o)$. Examination of the models that individually predict ΔH and ΔS further confirms the higher performance of the former, as foreshadowed by their validation MAEs (Section S1).

In the right column of Figure 3d, the same thermodynamic quantities are plotted vs. their most important feature as identified by their individual GBT models. As anticipated from the interpretability analysis (Figure 1c and Section S1), linear regression of $\ln(P_{eq}^o/P_o)$ and ΔH with $\bar{\nu}_{pa}$ yields large coefficients of determination with $R^2 > 0.9$. This specifically validates the first order design rules elucidated by the ML model and signifies that the greatest future improvements in model accuracy will come from improved ΔS predictions; however, this may require utilizing more sophisticated ML methods, accounting for specific crystallographic information in the featurization, relaxing the assumed temperature independence of ΔS, and/or obtaining more experimental training data. For example, the error on the ML predicted ΔS of AlTiVCr is larger than other compositions and could be due to the lack of

destabilization ($\Delta H \sim 40$ kJ/molH_2) in comparison to TiVZrNbHf ($\Delta H \sim 60$ kJ/molH_2). All alloys are synthesized as single-phase BCC SS (Figure 3a). Energy Dispersive X-Ray Scattering (EDS) maps of the as-synthesized and post-hydrided AlTiVNbTa sample are shown in Figure 3b. These EDS maps and the atomic fractions of elements shown in Table 1 indicate that elemental segregation is not observed post hydriding. Section S5.2.2 contains the complete spectra and experimental details.

Figure 3c shows absorption pressure-composition-temperature (PCT) data for TiVZrNbHf, AlTiVNbTa, and AlTiVCr. The measured plateau pressures for these new compositions immediately demonstrates the predicted destabilization trend, with c.a. two orders of magnitude increase in equilibrium pressure for AlTiVCr relative to TiVZrNbHf.
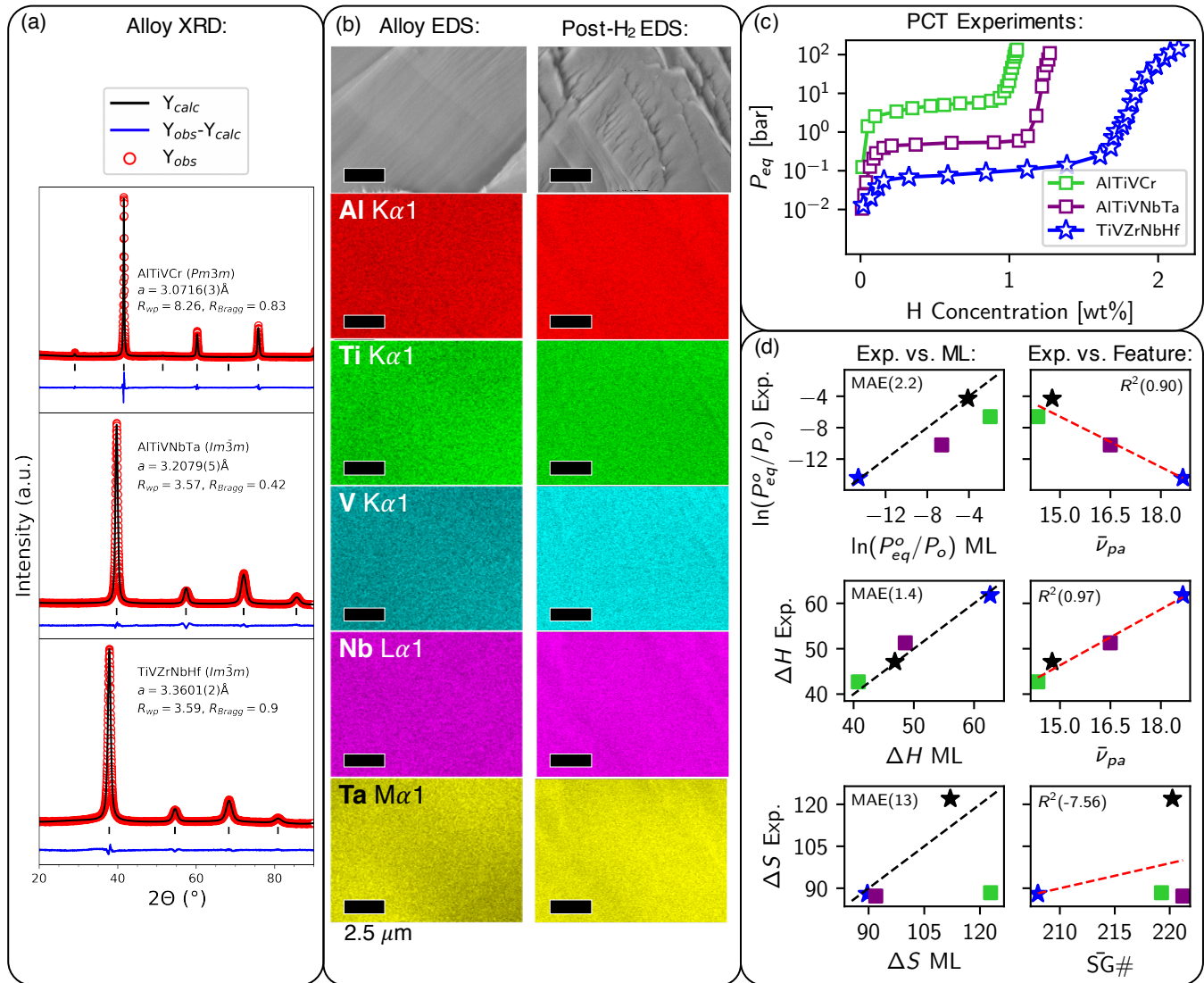
Figure 3: (a) XRD patterns of the as synthesized benchmark TiVZrNbHf and the novel compositions, AlTiVCr and AlTiVNbTa, synthesized in this work. (b) 10000x SEM/EDS maps for AlTiVNbTa. (c) Absorption PCT isotherms at 578 K, 561 K, and 571 K for TiVZrNbHf, AlTiVNbTa, and AlTiVCr, respectively. (d) Experimental hydriding thermodynamics vs. ML predictions (left column) and vs. the most important feature for each model (right column) with color-coding consistent with (c). Thermodynamic values for TiVCrNb were computed from the PCT data reported in Ref. 61 and included for comparison as black stars where the central temperature for the van't Hoff analysis was 100 °C.

training data in this region; we expect such predictions could be further improved when more experimental training data becomes available. The final database of all rHEA property predictions is provided in the Supplementary Files.

Corroborating rHEA thermodynamic trends with DFT. While compositional ML models are highly efficient for screening HEA phase behavior and hydride stability, DFT calculations can provide additional insight into the HEA hydriding reaction, in particular by probing local structure and favorable hydrogen binding sites. A "low-throughput" screening of HEA hydriding can be achieved for a handful of compositions to obtain similar qualitative insight as the compositional ML model, as well as more advanced mechanistic insight. For a given composition and BCC and FCC lattices, this workflow consists of relaxing a large number
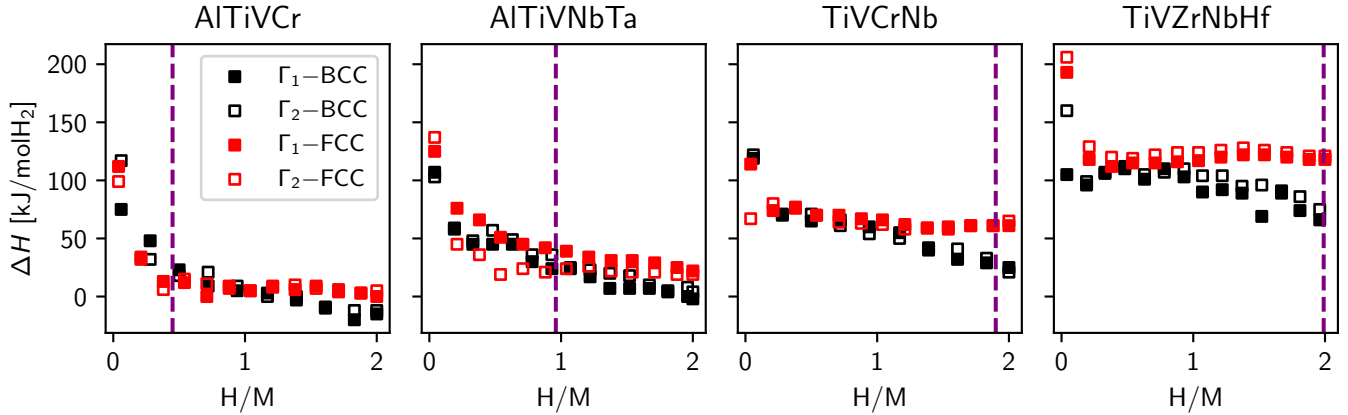
9

Figure 4: DFT calculated hydride desorption enthalpy as a function of hydrogen loading (H/M ratio) for different HEA compositions in either the BCC or FCC lattice. In order to probe the effect of metal distribution on calculated enthalpies, two alloy starting configurations were chosen (Γ_1 and Γ_2) as previously described. Dashed purple lines indicate the saturation H/M loading found for AlTiVCr, AlTiVNbTa, and TiVZrNbHf (Figure 3c) and for TiVCrNb (Ref. 61).

($\sim$100-300) of configurations with random SS site ordering. The configuration with the lowest formation energy Γ_1 and that with the median formation energy, Γ_2, are selected for hydriding. For a given Γ and a specified minimum possible H-H distance, d_{min} = 1.8 Å (chosen to be less than the Switendick criteria[62] while greater than experimentally measured exceptions to this rule[63]), hydrided structures at varying H/M ratios are produced as follows. All tetrahedral sites are identified and sorted from lowest to highest mean electronegativity of the surrounding lattice atoms. Hydrogen atoms are sequentially placed at these sites unless it is within d_{min} of an already placed H, in which case the site is skipped. After all tetrahedral sites are exhausted, the same procedure is repeated for octahedral holes that do not violate the d_{min} constraint. The hydrided structures are then relaxed, and the DFT energy of the hydrided lattice, E_{HEA+H_2}, the original alloy, E_{HEA}, and the gas phase H_2 molecule, E_{H_2}, can be used to approximate the desorption enthalpy at 0K for a structure with N hydrogen atoms,

$$\Delta H = \frac{1}{(N/2)}\left(E_{HEA} + (N/2)E_{H_2} - E_{HEA+H_2}\right). \tag{5}$$

Additional details on the DFT calculation settings are provided in Section S3.[42,64-67]

The results for TiVZrNbHf, TiVCrNb, Al-TiVNbTa, and AlTiVCr are summarized in Figure 4 and reveal several important mechanistic insights. First, the binding of hydrogen at low H/M concentrations is extremely favorable across the entire HEA series. Secondly, based on this screening procedure, the desorption enthalpy of Γ_1 and Γ_2 configurations for a given lattice type as a function of H/M remains similar, with the exception of the FCC lattice of Al-TiVNbTa. So, to first approximation, a higher energy starting configuration (Γ_2) does not have a significant impact on conclusions drawn from these computational predictions. Third, all HEAs here are synthesized as single-phase BCC SS alloys (Figure 3a and Ref. 61) and TiVCrNb and TiVZrNbHf were shown to exhibit a BCC to FCC transition upon hydriding.[43] This is reproduced by DFT since, beyond some critical concentration typically around H/M=1, the stability of the FCC lattice is significantly increased (higher desorption enthalpy) relative to the BCC lattice. This implies that the hydriding enthalpy is the thermodynamic driving force for the experimentally observed BCC to FCC phase transition. Finally, regardless of lattice type or configuration, the DFT-predicted ΔH exhibits the same qualitative trend of increased stability across TiVZrNbHf > AlTiVNbTa > AlTiVCr. For two materials like AlTiVNbTa and TiVCrNb that have very similar experimentally measured ΔH but significantly dif-

10

ferent capacities, Figure 4 effectively illustrates that the FCC hydride remains much more stable at higher H/M than that of AlTiVNbTa, which continues to decrease in stability as H/M increases.

Next, we show the DFT calculated formation energies (in meV/atom) of alloys and hydrides (with H/M=2) with respect to elemental reference in Figure 5. These calculations are for the Γ_1 configuration. For the HEAs lacking Al, the formation energies of the metal alloys are positive, indicating that entropic contributions stabilize the SS phase. The formation energies of the FCC hydride (at H/M=2) are lower than that of the BCC hydride phase, again a qualitative signature for the BCC to FCC phase transition upon hydrogenation as observed experimentally in several of the HEA compositions.[46] Most importantly, we observe the general trend of less stable alloys leading to more stable hydrides across all HEA compositions considered, which follows the common rule of alloy-hydride reversed stability discussed extensively in experimental and computational studies on intermetallic hydrides.[31,68] Such correlation, in combination with the ML models which we discussed earlier, provides qualitative design trends to target HEAs with desired hydriding thermodynamics.
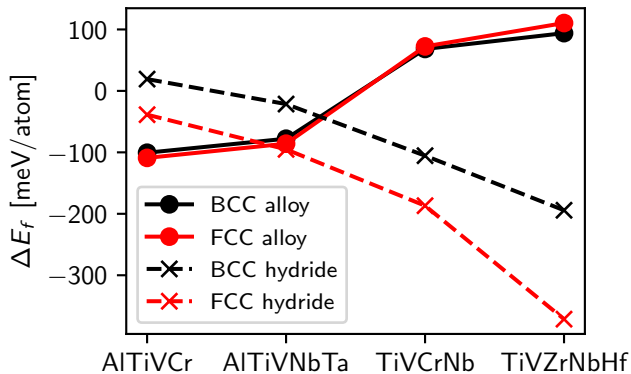

Figure 5: DFT calculated formation energies (in meV/atom) of alloys and hydrides (with H/M=2) with respect to elemental reference. Calculations are for the Γ_1 configuration.

Ultimately, these calculations can be utilized as a first-order screening method to reproduce ML and experimental stability trends and to gain atomistic understanding of preferred hydrogen binding sites and energies. Moreover, while our ML models currently only support thermodynamic property predictions, this DFT analysis adds qualitative insights in hydriding capacity. To achieve rigorous and quantitative prediction of hydride stability, i.e. equilibrium pressure, at the DFT level of accuracy for a large number of HEAs, however, will require significant computational efficiency advancements. A link is provided in Section S4 to our toolkit that generates the HEA hydride structures used in the DFT analysis above.

Conclusions

The wide ranging tunability of HEAs presents an intractably large design/composition space for brute force experimentation or high-throughput calculation of expensive-to-compute properties (i.e., the hydriding equilibrium pressure at an *ab initio* theory level). With the goal of efficiently predicting and synthesizing novel HEA hydrides that are destabilized relative to TiVZrNbHf, a different approach is clearly needed. We therefore trained an explainable ML model on the HydPARK database of metal hydride thermodynamic properties, and, through additional data and features, systematically improved the model in order to high-throughput screen the hydriding thermodynamics of 672 rHEA materials. After applying secondary selection criteria, including a separate model that predicted the alloy's single-phase SS formation, several novel compositions were experimentally synthesized. The measured hydriding thermodynamics not only reproduced the predicted trend in hydride destabilization, but also validated the simple, first-order design rules elucidated by the explainable ML model. With AlTiVCr, a ΔH decrease in 20 kJ/molH$_2$ was both predicted and observed relative to TiVZrNbHf, leading to a $\sim$ 70x increase in the plateau pressure. In addition to these fundamental insights, this work provides practically important knowledge: namely, a large, open-source HEA

dataset where the desired equilibrium pressure spans orders of magnitude but can be finely and continuously tuned. This type of information is a necessity to enable technologies like metal hydride hydrogen compressors, for example, which require a series of hydrides exhibiting specifically targeted, increasing equilibrium pressures across a wide range.

Significant opportunities remain to improve the search for optimal HEAs for hydrogen storage across different applications. For example, continued experimentation is required to provide more ML training data on compositions beyond the current scope of the rHEA dataset.[69] Predictive power over a wider HEA compositional space could lead to the discovery of materials that simultaneously exhibit thermodynamic destabilization without sacrificing capacity, a trade-off that was clearly observed with TiVZrNbHf, AlTiVCr, and AlTiVNbTa and elsewhere.[43] We additionally performed a DFT screening procedure to probe ΔH of HEA hydrides. Importantly, this DFT screening procedure is computationally tractable and reproduced the destabilization trend predicted by ML and shown by experiments, while simultaneously providing more atomistic insight into the hydriding process. If HEA hydride thermodynamic data can be continually collected (either experimentally or computationally) and stored in centralized, standardized repositories,[70] the quality of ML thermodynamic models will be further improved. This will lead to rapid progress in the nascent search for lighter, destabilized HEA hydrides with higher gravimetric delivery at milder conditions. In this spirit, the code and data to retrain all ML models, as well as the final database of rHEA predicted properties, is provided open source.

Supporting Information

The Supporting Information is available free of charge.

- Thermodynamic model details (Section S1); Phase prediction model details (Section S2); DFT settings (Section S3); Code availability (Section S4); Experimental methods (Section S5)

References

(1) IPCC, *An IPCC Special Report on the impacts of global warming of 1.5°C*; 2018; pp 674–684.

(2) Züttel, A.; Remhof, A.; Borgschulte, A.; Friedrichs, O. Hydrogen: the future energy carrier. *Philos. Trans. R. Soc. A Math. Phys. Eng. Sci.* **2010**, *368*, 3329–3342.

(3) Schlapbach, L.; Züttel, A. Hydrogen-storage materials for mobile applications. *Nature* **2001**, *414*, 353–358.

(4) Reilly, J. Chemistry of Intermetallic Hydrides. 180th Meet. Electrochem. Soc. 1991.

(5) Mohtadi, R.; Orimo, S. I. The renaissance of hydrides as energy materials. *Nat. Rev. Mater.* **2016**, *2*, 1–16.

(6) Bellosta von Colbe, J. et al. Application of hydrides in hydrogen storage and compression: Achievements, outlook and perspectives. *Int. J. Hydrogen Energy* **2019**, *44*, 7780–7808.

(7) Reilly, J. J.; Wiswall, R. H. Formation and properties of iron titanium hydride. *Inorg. Chem.* **1974**, *13*, 218–222.

(8) Orimo, S.-i.; Nakamori, Y.; Eliseo, J. R.; Züttel, A.; Jensen, C. M. Complex Hydrides for Hydrogen Storage. *Chem. Rev.* **2007**, *107*, 4111–4132.

(9) Milanese, C.; Jensen, T.; Hauback, B.; Pistidda, C.; Dornheim, M.; Yang, H.; Lombardo, L.; Zuettel, A.; Filinchuk, Y.; Ngene, P.; de Jongh, P.; Buckley, C.; Dematteis, E.; Baricco, M. Complex hydrides for energy storage. *Int. J. Hydrogen Energy* **2019**, *44*, 7860–7874.

(10) Reilly, J. J.; Wiswall, R. H. Reaction of hydrogen with alloys of magnesium and nickel and the formation of Mg_2NiH_4. *Inorg. Chem.* **1968**, *7*, 2254–2256.

(11) Vajo, J. J.; Mertens, F.; Ahn, C. C.; Bowman, R. C.; Fultz, B. Altering Hydrogen Storage Properties by Hydride Destabilization through Alloy Formation: LiH and MgH_2 Destabilized with Si. *J. Phys. Chem. B* **2004**, *108*, 13977–13983.

(12) Wang, P.; Jensen, C. Method for preparing Ti-doped NaAlH4 using Ti powder: observation of an unusual reversible dehydrogenation behavior. *J. Alloys Compd.* **2004**, *379*, 99–102.

(13) Alapati, S. V.; Johnson, J. K.; Sholl, D. S. Identification of Destabilized Metal Hydrides for Hydrogen Storage Using First Principles Calculations. *J. Phys. Chem. B* **2006**, *110*, 8769–8776.

(14) Walker, G. S.; Abbas, M.; Grant, D. M.; Udeh, C. Destabilisation of magnesium hydride by germanium as a new potential multicomponent hydrogen storage system. *Chem. Commun.* **2011**, *47*, 8001.

(15) Cahen, S.; Eymery, J.-B.; Janot, R.; Tarascon, J.-M. Improvement of the LiBH4 hydrogen desorption by inclusion into mesoporous carbons. *J. Power Sources* **2009**, *189*, 902–908.

(16) Bhakta, R. K.; Herberg, J. L.; Jacobs, B.; Highley, A.; Behrens, R.; Ockwig, N. W.; Greathouse, J. A.; Allendorf, M. D. Metal−Organic Frameworks As Templates for Nanoscale $NaAlH_4$. *J. Am. Chem. Soc.* **2009**, *131*, 13198–13199.

(17) Schneemann, A.; White, J. L.; Kang, S.; Jeong, S.; Wan, L. F.; Cho, E. S.; Heo, T. W.; Prendergast, D.; Urban, J. J.; Wood, B. C.; Allendorf, M. D.; Stavila, V. Nanostructured Metal Hydrides for Hydrogen Storage. *Chem. Rev.* **2018**, *118*, 10775–10839.

(18) Wood, B. C.; Stavila, V.; Poonyayant, N.; Heo, T. W.; Ray, K. G.; Klebanoff, L. E.; Udovic, T. J.; Lee, J. R. I.; Angboonpong, N.; Sugar, J. D.; Pakawatpanurut, P. Nanointerface-Driven Reversible Hydrogen Storage in the Nanoconfined Li-N-H System. *Adv. Mater. Interfaces* **2017**, *4*, 1600803.

(19) Yeh, J.-W.; Chen, S.-K.; Lin, S.-J.; Gan, J.-Y.; Chin, T.-s.; Shun, T.-T.; Tsau, C.-h.; Chang, S.-Y. Nanostructured High-Entropy Alloys with Multiple Principal Elements: Novel Alloy Design Concepts and Outcomes. *Adv. Eng. Mater.* **2004**, *6*, 299–303.

(20) Shafeie, S.; Guo, S.; Hu, Q.; Fahlquist, H.; Erhart, P.; Palmqvist, A. High-entropy

alloys as high-temperature thermoelectric materials. *J. Appl. Phys.* **2015**, *118*, 184905.

(21) Gao, M. C.; Yeh, J.-w.; Liaw, P. K.; Zhang, Y. *High-Entropy Alloys*; Springer International Publishing, 2016; pp 1–20.

(22) George, E. P.; Raabe, D.; Ritchie, R. O. High-entropy alloys. *Nat. Rev. Mater.* **2019**, *4*, 515–534.

(23) Tran, A.; Tranchida, J.; Wildey, T.; Thompson, A. P. Multi-fidelity machine-learning with uncertainty quantification and Bayesian optimization for materials design: Application to ternary random alloys. *J. Chem. Phys.* **2020**, *153*, 1–9.

(24) Melia, M. A.; Whetten, S. R.; Puckett, R.; Jones, M.; Heiden, M. J.; Argibay, N.; Kustas, A. B. High-throughput additive manufacturing and characterization of refractory high entropy alloys. *Appl. Mater. Today* **2020**, *19*.

(25) Xin, Y.; Li, S.; Qian, Y.; Zhu, W.; Yuan, H.; Jiang, P.; Guo, R.; Wang, L. High-Entropy Alloys as a Platform for Catalysis: Progress, Challenges, and Opportunities. *ACS Catal.* **2020**, *10*, 11280–11306.

(26) Sahlberg, M.; Karlsson, D.; Zlotea, C.; Jansson, U. Superior hydrogen storage in high entropy alloys. *Sci. Rep.* **2016**, *6*, 36770.

(27) Westlake, D. Hydrides of intermetallic compounds: A review of stabilities, stoichiometries and preferred hydrogen sites. *J. Less Common Met.* **1983**, *91*, 1–20.

(28) Cuevas, F.; Joubert, J.-M.; Latroche, M.; Percheron-Guégan, A. Intermetallic compounds as negative electrodes of Ni/MH batteries. *Appl. Phys. A Mater. Sci. Process.* **2001**, *72*, 225–238.

(29) Wolverton, C.; Siegel, D. J.; Akbarzadeh, A. R.; Ozoliņš, V. Discovery of novel hydrogen storage materials: an atomic scale computational approach. *J. Phys. Condens. Matter* **2008**, *20*, 064228.

(30) Hattrick-Simpers, J. R.; Choudhary, K.; Corgnale, C. A simple constrained machine learning model for predicting high-pressure-hydrogen-compressor materials. *Mol. Syst. Des. Eng.* **2018**, *3*, 509–517.

(31) Witman, M.; Ling, S.; Grant, D. M.; Walker, G. S.; Agarwal, S.; Stavila, V.; Allendorf, M. D. Extracting an Empirical Intermetallic Hydride Design Principle from Limited Data via Interpretable Machine Learning. *J. Phys. Chem. Lett.* **2020**, *11*, 40–47.

(32) Goel, H.; Ling, S.; Ellis, B. N.; Taconi, A.; Slater, B.; Rai, N. Predicting vapor liquid equilibria using density functional theory: A case study of argon. *J. Chem. Phys.* **2018**, *148*, 224501.

(33) Ward, L.; Agrawal, A.; Choudhary, A.; Wolverton, C. A general-purpose machine learning framework for predicting properties of inorganic materials. *npj Comput. Mater.* **2016**, *2*, 16028.

(34) Goodall, R. E. A.; Lee, A. A. Predicting materials properties without crystal structure: deep representation learning from stoichiometry. *Nat. Commun.* **2020**, *11*, 6280.

(35) Bartel, C. J.; Trewartha, A.; Wang, Q.; Dunn, A.; Jain, A.; Ceder, G. A critical examination of compound stability predictions from machine-learned formation energies. *npj Comput. Mater.* **2020**, *6*, 97.

(36) Lototsky, M.; Yartys, V.; Klochko, Y.; Borisko, V.; Starovoitov, R.; Azhazha, V.; V'yugov, P. Applications of Zr–V hydrogen getters in vacuum-plasma devices: Phase-structural and hydrogen sorption characteristics. *J. Alloys Compd.* **2005**, *404-406*, 724–727.

(37) Lototskyy, M.; Yartys, V.; Pollet, B.; Bowman, R. Metal hydride hydrogen com-

pressors: A review. *Int. J. Hydrogen Energy* **2014**, *39*, 5818–5851.

(38) Yartys, V. A.; Lototskyy, M.; Linkov, V.; Grant, D.; Stuart, A.; Eriksen, J.; Denys, R.; Bowman, R. C. Metal hydride hydrogen compression: recent advances and future prospects. *Appl. Phys. A* **2016**, *122*, 415.

(39) Coelho, A. A. TOPAS and TOPAS-Academic : an optimization program integrating computer algebra and crystallographic objects written in C++. *J. Appl. Crystallogr.* **2018**, *51*, 210–218.

(40) Thompson, P.; Cox, D. E.; Hastings, J. B. Rietveld refinement of Debye–Scherrer synchrotron X-ray data from Al_2O_3. *J. Appl. Crystallogr.* **1987**, *20*, 79–83.

(41) Pedregosa, F. et al. Scikit-learn: Machine Learning in Python. *Journal of Machine Learning Research* **2011**, *12*, 2825–2830.

(42) Kresse, G.; Furthmüller, J. Efficient iterative schemes for ab initio total-energy calculations using a plane-wave basis set. *Phys. Rev. B* **1996**, *54*, 11169–11186.

(43) Nygård, M. M.; Ek, G.; Karlsson, D.; Sørby, M. H.; Sahlberg, M.; Hauback, B. C. Counting electrons - A new approach to tailor the hydrogen sorption properties of high-entropy alloys. *Acta Mater.* **2019**, *175*, 121–129.

(44) Zlotea, C.; Sow, M.; Ek, G.; Couzinié, J.-P.; Perrière, L.; Guillot, I.; Bourgon, J.; Møller, K.; Jensen, T.; Akiba, E.; Sahlberg, M. Hydrogen sorption in TiZrNbHfTa high entropy alloy. *J. Alloys Compd.* **2019**, *775*, 667–674.

(45) Kunce, I.; Polanski, M.; Bystrzycki, J. Microstructure and hydrogen storage properties of a TiZrNbMoV high entropy alloy synthesized using Laser Engineered Net Shaping (LENS). *Int. J. Hydrogen Energy* **2014**, *39*, 9904–9910.

(46) Ek, G.; Nygård, M. M.; Pavan, A. F.; Montero, J.; Henry, P. F.; Sørby, M. H.; Witman, M.; Stavila, V.; Zlotea, C.; Hauback, B. C.; Sahlberg, M. Elucidating the Effects of the Composition on Hydrogen Sorption in TiVZrNbHf-Based High-Entropy Alloys. *Inorg. Chem.* **2021**, *60*, 1124–1132.

(47) Miracle, D.; Senkov, O. A critical review of high entropy alloys and related concepts. *Acta Mater.* **2017**, *122*, 448–511.

(48) Hastie, T.; Tibshirani, R.; Friedman, J. *The Elements of Statistical Learning*; Springer New York, 2009; pp 337–388.

(49) Ong, S. P.; Richards, W. D.; Jain, A.; Hautier, G.; Kocher, M.; Cholia, S.; Gunter, D.; Chevrier, V. L.; Persson, K. A.; Ceder, G. Python Materials Genomics (pymatgen): A robust, open-source python library for materials analysis. *Comput. Mater. Sci.* **2013**, *68*, 314–319.

(50) Jain, A.; Ong, S. P.; Hautier, G.; Chen, W.; Richards, W. D.; Dacek, S.; Cholia, S.; Gunter, D.; Skinner, D.; Ceder, G.; Persson, K. A. Commentary: The Materials Project: A materials genome approach to accelerating materials innovation. *APL Mater.* **2013**, *1*, 011002.

(51) Lundberg, S.; Lee, S.-I. A Unified Approach to Interpreting Model Predictions. *Adv. Neural Inf. Process. Syst.* **2017**, 4766–4775.

(52) Lundberg, S. M.; Erion, G. G.; Lee, S.-I. Consistent Individualized Feature Attribution for Tree Ensembles. 2019-03-07. *arXiv:1802.03888v3* (accessed 2020–09–02).

(53) Okada, M.; Kuriiwa, T.; Tamura, T.; Takamura, H.; Kamegawa, A. Ti–V–Cr b.c.c. alloys with high protium content. *J. Alloys Compd.* **2002**, *330-332*, 511–516.

(54) Senkov, O. N.; Miller, J. D.; Miracle, D. B.; Woodward, C. Accelerated exploration of multi-principal element alloys with solid solution phases. *Nat. Commun.* **2015**, *6*, 1–10.

(55) Senkov, O.; Miller, J.; Miracle, D.; Woodward, C. Accelerated exploration of multi-principal element alloys for structural applications. *Calphad* **2015**, *50*, 32–48.

(56) Gao, M.; Zhang, C.; Gao, P.; Zhang, F.; Ouyang, L.; Widom, M.; Hawk, J. Thermodynamics of concentrated solid solution alloys. *Curr. Opin. Solid State Mater. Sci.* **2017**, *21*, 238–251.

(57) Guo, S.; Ng, C.; Lu, J.; Liu, C. T. Effect of valence electron concentration on stability of fcc or bcc phase in high entropy alloys. *J. Appl. Phys.* **2011**, *109*.

(58) Guo, S.; Hu, Q.; Ng, C.; Liu, C. More than entropy in high-entropy alloys: Forming solid solutions or amorphous phase. *Intermetallics* **2013**, *41*, 96–103.

(59) Huang, W.; Martin, P.; Zhuang, H. L. Machine-learning phase prediction of high-entropy alloys. *Acta Mater.* **2019**, *169*, 225–236.

(60) Agarwal, S.; Hudson, C. M. Probability Series Expansion Classifier that is Interpretable by Design. 2017-10-27. *arXiv:1710.10301v1* (accessed 2019–08–01).

(61) Nygård, M. M.; Fjellvåg, Ø. S.; Sørby, M. H.; Sakaki, K.; Ikeda, K.; Armstrong, J.; Vajeeston, P.; Sławiński, W. A.; Kim, H.; Machida, A.; Nakamura, Y.; Hauback, B. C. The average and local structure of TiVCrNbD$_x$ (x=0;2:2;8) from total scattering and neutron spectroscopy. *Acta Mater.* **2021**, *205*, 116496.

(62) Switendick, A. C. Band Structure Calculations for Metal Hydrogen Systems*. *Zeitschrift für Phys. Chemie* **1979**, *117*, 89–112.

(63) Borgschulte, A.; Terreni, J.; Billeter, E.; Daemen, L.; Cheng, Y.; Pandey, A.; Łodziana, Z.; Hemley, R. J.; Ramirez-Cuesta, A. J. Inelastic neutron scattering evidence for anomalous H–H distances in metal hydrides. *Proc. Natl. Acad. Sci.* **2020**, *117*, 4021–4026.

(64) Blöchl, P. E. Projector augmented-wave method. *Phys. Rev. B* **1994**, *50*, 17953–17979.

(65) Hobbs, D.; Kresse, G.; Hafner, J. Fully unconstrained noncollinear magnetism within the projector augmented-wave method. *Phys. Rev. B* **2000**, *62*, 11556–11570.

(66) Perdew, J. P.; Burke, K.; Ernzerhof, M. Generalized Gradient Approximation Made Simple. *Phys. Rev. Lett.* **1996**, *77*, 3865–3868.

(67) Methfessel, M.; Paxton, A. T. High-precision sampling for Brillouin-zone integration in metals. *Phys. Rev. B* **1989**, *40*, 3616–3621.

(68) Van Mal, H.; Buschow, K.; Miedema, A. Hydrogen absorption in LaNi$_5$ and related compounds: Experimental observations and their explanation. *J. Less Common Met.* **1974**, *35*, 65–76.

(69) Montero, J.; Ek, G.; Sahlberg, M.; Zlotea, C. Improving the hydrogen cycling properties by Mg addition in Ti-V-Zr-Nb refractory high entropy alloy. *Scr. Mater.* **2021**, *194*, 113699.

(70) Coudert, F. Materials Databases: The Need for Open, Interoperable Databases with Standardized Data and Rich Metadata. *Adv. Theory Simulations* **2019**, 1900131.

Graphical TOC Entry